



# Microstructural evolution and thermal stability of HfN/ScN, ZrN/ScN, and Hf<sub>0.5</sub>Zr<sub>0.5</sub>N/ScN metal/semiconductor superlattices

Magnus Garbrecht<sup>1,\*</sup> , Jeremy L. Schroeder<sup>1</sup>, Lars Hultman<sup>1</sup>, Jens Birch<sup>1</sup>, Bivas Saha<sup>2</sup>, and Timothy D. Sands<sup>3,4</sup>

<sup>1</sup>Thin Film Physics Division, Department of Physics, Chemistry and Biology, Linköping University, 581 83 Linköping, Sweden

<sup>2</sup>Department of Materials Science and Engineering, University of California, Berkeley, CA 94720, USA

<sup>3</sup>Bradley Department of Electrical and Computer Engineering, Virginia Tech, Blacksburg, VA 24061, USA

<sup>4</sup>Department of Materials Science and Engineering, Virginia Tech, Blacksburg, VA 24061, USA

Received: 18 April 2016

Accepted: 24 May 2016

Published online:

2 June 2016

© Springer Science+Business Media New York 2016

## ABSTRACT

Nitride-based metal/semiconductor superlattices for possible applications as thermoelectric, plasmonic, and hard coating materials have been grown by magnetron sputtering. Since long-time thermal stability of the superlattices is crucial for these applications, the atomic scale microstructure and its evolution under annealing to working temperatures were investigated with high-resolution transmission electron microscopy methods. We report on epitaxial growth of three cubic superlattice systems (HfN/ScN, ZrN/ScN, and Hf<sub>0.5</sub>Zr<sub>0.5</sub>N/ScN) that show long-time thermal stability (annealing up to 120 h at 950 °C) as monitored by scanning transmission electron microscopy-based energy-dispersive X-ray spectroscopy. No interdiffusion between the metal and semiconductor layers could be observed for any of the present systems under long-time annealing, which is in contrast to earlier attempts on similar superlattice structures based on TiN as the metallic compound. Atomically resolved high-resolution transmission electron microscopy imaging revealed that even though the superlattice curves towards the substrate at regular interval column boundaries originating from threading dislocations close to the substrate interface, the cubic lattice continues coherently across the boundaries. It is found that the boundaries themselves are alloyed along the entire growth direction, while in their vicinity nanometer-size inclusions of metallic phases are observed that could be identified as the zinc blende phase of same stoichiometry as the parent rock salt transition metal nitride phase. Our results demonstrate the long-time thermal stability of metal/semiconductor superlattices based on Zr and Hf nitrides.

Address correspondence to E-mail: magnus.garbrecht@liu.se

## Introduction

The growth and development of metal/semiconductor superlattices with low defect densities for applications as hard coatings, high-temperature thermoelectric, and plasmonic materials has been a focus of scientific interest for a long time. In the 1960s, motivated by the prospect of developing quantum electronic devices, Jaklevic and Jambe [1, 2] performed seminal tunneling experiments on metal–insulator–metal (MIM) structures based on polycrystalline Al/Al<sub>2</sub>O<sub>3</sub>/Pb heterojunctions. In the 1980s, Sands and Palmstrom et al. [3–5] conducted similar experiments when they developed AlAs/NiAl/AlAs and GaAs/ErAs/GaAs semiconductor/metal/semiconductor heterojunctions for metal base and permeable base transistors. More recently, metal/semiconductor multilayers based on elemental metals and semiconductors have been developed and utilized to demonstrate novel optical metamaterials [6]. However, these examples of heteroepitaxial metal/semiconductor superlattices are not amenable to atomic scale control of interfaces because of the crystal structure, lattice constant, and space group mismatch among constituents.

We recently reported on the development of the first epitaxial metal/semiconductor superlattices based on TiN/(Al,Sc)N with low defect densities on MgO (001) substrates [7, 8]. These artificially structured materials are nominally single crystalline, possess sharp interfaces, and exhibit high melting temperatures and mechanical hardness. Their potential suitability for thermoelectric and plasmonic metamaterial applications has been explored [9–11]. These novel superlattices may also be suitable for applications in refractory electronic and refractory plasmonic devices due to their hardness, chemical stability, and high melting temperature of transition metal nitrides. Their properties are moreover tunable by alloying, doping, and quantum size effects. For instance, the cross-plane thermal conductivity could be significantly reduced in alloyed systems with nominal stoichiometry of Ti<sub>0.7</sub>W<sub>0.3</sub>N/Al<sub>0.72</sub>Sc<sub>0.28</sub>N [9].

However, scanning/transmission electron microscopy (S/TEM)-based energy-dispersive X-ray spectroscopy (EDX) studies on the TiN/(Al,Sc)N-based systems revealed that the metastable rock salt Al<sub>0.72</sub>Sc<sub>0.28</sub>N layers in the superlattices undergo a rock salt-to-wurtzite structural phase transformation at high temperatures (1000 °C) that leads to a loss of epitaxy

and significant intermixing at the interfaces. The microscopic study also demonstrated that a significant amount of metal atom diffusion between the metal and semiconductor layers occurs after annealing the superlattices to 950 °C for more than 24 h [12]. Since working temperatures of up to 1000 °C are common for applications in both high-temperature thermoelectric materials [13, 14] and hard coatings of cutting tools [15, 16], maintaining long-time thermal stability under such working conditions is crucial for any candidate system.

Consequently, we further developed the nitride-based metal/semiconductor superlattices from previous works by variation of the metal species and stoichiometry, and those are presented here. Combining aberration-corrected high-resolution (HR) S/TEM imaging and EDX mapping proved to be an optimal tool for the investigation of the thermal stability of the superlattices as well as phase purity, quality of interfaces, and film morphology [9, 12].

In the present work, we present HRS/TEM-based results on three metal/semiconductor superlattices (HfN/ScN, ZrN/ScN, and Hf<sub>0.5</sub>Zr<sub>0.5</sub>N/ScN) grown by magnetron sputtering. High-resolution EDX mapping in aberration-corrected STEM mode highlights significantly improved thermal stability of the (Hf,Zr)N/ScN-based superlattices compared to previous thermal stability studies on TiN/ScN-based superlattices [12]. Moreover, interface quality, phase purity, film morphology and microstructure, and evolution under annealing were investigated by atomically resolved S/TEM analysis.

## Experimental

### Film growth and treatment

(Hf,Zr)N/ScN thin-film superlattices were grown on 001-oriented MgO substrates with a reactive DC magnetron sputtering technique inside a load-locked turbomolecular-pumped high-vacuum deposition system with a base pressure of 10<sup>-8</sup> torr (PVD Products, Inc.). The growth chamber had the capability to accommodate four targets and was equipped with three DC power supplies. The Sc (99.998 % purity), Zr (99.99 %), and Hf (99.99 %) targets had the dimensions of 2 in. diameter and 0.25 in. thickness. All depositions were performed with an Ar/N<sub>2</sub> mixture having 6 sccm of N<sub>2</sub> and 4 sccm of Ar at a

deposition pressure of 5 mTorr. The targets were sputtered in constant power mode, with Sc, Hf, and Zr power held constant at 200 W for the binary superlattices, but varied slightly for the (Zr,Hf)N system to achieve the desired concentration. The deposition rates were  $4.2 \text{ nm min}^{-1}$  for ScN,  $5.1 \text{ nm min}^{-1}$  for HfN, and  $4.8 \text{ nm/min}$  for ZrN. The substrates were maintained at  $850 \text{ }^\circ\text{C}$  during deposition, as determined using an infrared pyrometer operated in the wavelength range of  $0.8\text{--}1.1 \text{ }\mu\text{m}$ , together with a thermocouple. Three superlattice samples were deposited for the thermal stability study. The film structures with nominal values are as follows:

1. 200 nm HfN buffer/ $1 \text{ }\mu\text{m}$  6 nm/6 nm HfN/ScN superlattice/20 nm HfN capping layer,
2. 200 nm ZrN buffer/ $1 \text{ }\mu\text{m}$  6 nm/6 nm ZrN/ScN superlattice/20 nm ZrN capping layer, and
3. 200 nm HfN/ $1 \text{ }\mu\text{m}$  6 nm/6 nm (Hf<sub>0.5</sub>Zr<sub>0.5</sub>)N/ScN superlattice/20 nm HfN capping layer.

The superlattices were annealed (ramp rate =  $20 \text{ }^\circ\text{C min}^{-1}$ ) at  $950 \text{ }^\circ\text{C}$  for either 24 h or 120 h in a  $1.1 \text{ Pa}$  ( $8.5 \text{ mTorr}$ ) forming gas ambient (5 % H<sub>2</sub>:95 % N<sub>2</sub>). The custom-designed annealing furnace consisted of a Boralectric tube heater inside a vacuum chamber that was evacuated to  $<9.3 \times 10^{-5} \text{ Pa}$  ( $7 \times 10^{-7} \text{ Torr}$ ) before continuously flowing 30 sccm forming gas to achieve a pressure of  $8.5 \text{ mTorr}$ . The  $950 \text{ }^\circ\text{C}$  temperature of the inside heater wall and sample were verified with a dual-wavelength pyrometer (CellaTemp PA40;  $0.95$  and  $1.05 \text{ }\mu\text{m}$ ).

### Electron microscopy methods

All experiments were conducted with Linköping's image- and probe-corrected and monochromated FEI Titan<sup>3</sup> 60–300 microscope equipped with a Gatan Quantum ERS GIF, high-brightness XFEG source, and Super-X EDX detector for ultra-high count rates, operated at 300 kV. The Super-X EDX detector system exhibits count rates that are two orders of magnitude greater than conventional systems, thereby enabling the recording of spatially resolved high-resolution EDX maps within a few minutes. The EDX maps contain arrays of individual spectra (typically  $250 \times 250$  for the maps presented here), one per pixel, and by color coding, the elemental peak of the highest intensity for each spectrum/pixel is shown in

the map. Those individual spectra can then be integrated for area-specific quantification.

Negative spherical aberration contrast imaging (NCSI) is an enhanced contrast transfer technique that is capable of resolving the atomic lattice structure of even complex systems with accuracies of a few picometers [17–21]. Hence, for HRTEM imaging, the image corrector of the microscope was tuned to yield a negative spherical aberration coefficient (Cs) of ca.  $-8 \text{ }\mu\text{m}$ , and micrographs were recorded with a small positive defocus (Z) of a few nm producing NCSI images for direct interpretability of intensity maxima as atomic column positions. For HRSTEM and EDX mapping, the probe corrector was used to form a focused probe of less than  $1 \text{ \AA}$  diameter, which defines the resolution in scanning mode.

High-resolution image contrast simulations were performed with the JEMS software package [22], utilizing multislice algorithms and matching the experimental imaging conditions and measured optical aberrations.

Cross-section TEM samples were prepared conventionally by face-to-face mounting and gluing of two slices of the film/substrate samples followed by mechanical thinning and polishing employing a tripod tool. Thinning to electron transparency was achieved by room-temperature ion beam milling using a Gatan PIPS ion mill with  $5 \text{ keV Ar}^+$  ions at the incidence angles of  $8^\circ\text{--}10^\circ$  with respect to the sample surface. Subsequent polishing was achieved in a Technoorg Linda ion mill by gradually decreasing the  $\text{Ar}^+$  ion energy from 1 kV to 250 eV to minimize surface amorphization.

## Results and discussion

### Film microstructure and evolution

The microstructures of the as-deposited ZrN/ScN, HfN/ScN, and Hf<sub>0.5</sub>Zr<sub>0.5</sub>N/ScN films appear very similar to each other as can be seen from cross-sectional overview micrographs showing the entire superlattice stack. Grown on a 200-nm layer of their respective metal nitride compound, the films are about  $1 \text{ }\mu\text{m}$  thick with alternating metal and semiconductor layers of average  $\sim 6.5 \text{ nm}$  thickness. However, individually higher thicknesses of up to  $10 \text{ nm}$  can be found.

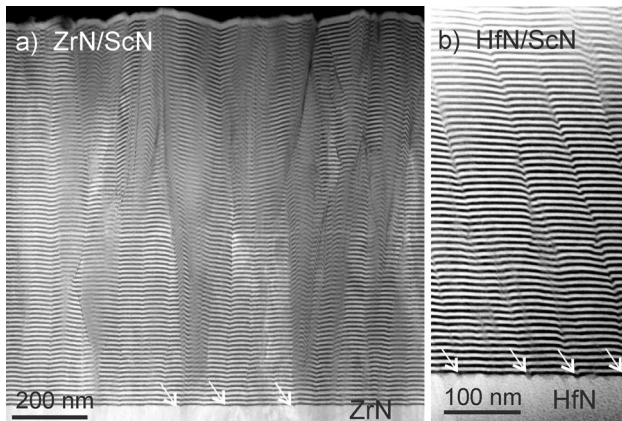


**Figure 1** Low-magnification HAADF-STEM micrographs showing the as-deposited metal/semiconductor superlattice film of **a** ZrN/ScN in its entirety and **b** the region adjacent to the substrate for the HfN/ScN stack. *Arrows* point at surface cusp defects located at the interface from which columnar boundaries extend effectively vertically up towards the film surface.

Figure 1 shows cross-sectional high-angle annular dark-field (HAADF)-STEM micrographs of the entire superlattice stack for the as-deposited ZrN/ScN (a) and a closer detail of the region adjacent to the MgO substrate for the as-deposited HfN/ScN. Since HAADF-STEM mode produces (atomic number) Z-contrast-sensitive intensity distributions, the bright contrast areas depict the metal layers, which contain the heavy elements Zr (a) and Hf (b), respectively.

Columnar grain boundaries at the intervals of a few tens to hundreds of nanometers extend almost vertically throughout the entire film perpendicular to the substrate/film interface. Moreover, as can be seen in Fig. 1b, the layers curve towards the substrate in the direct vicinity of the boundaries, forming V-shaped kinks.

Columnar boundaries of that kind are well known to appear in nitride films prepared by magnetron sputtering, originating from threading dislocations forming at the substrate/film interface as a result of surface cusps on the substrate during growth [23, 24].

Indeed, the surface of the 200-nm HfN stack in Fig. 1b clearly shows the respective defects, some of which are marked by arrows. The faint contrast lines in Fig. 1a reaching down through the ZrN stack towards the MgO substrate (not in the image) show furthermore that the origin of some of the boundaries is found at the substrate/film interface, as expected.

The evolution of the microstructure of HfN/ScN under annealing at 950 °C can be seen in the

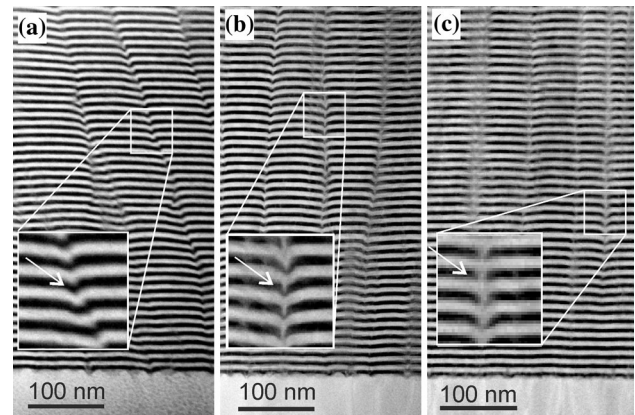


**Figure 2** Low-magnification HAADF-STEM micrographs showing the lower part of the as-deposited (a), 24-h (b), and 120-h (c) annealed (at 950 °C) HfN/ScN superlattice. The *insets* show the formation of vertical bridges of heavy atoms between the metallic HfN layers at the boundaries (b), resulting ultimately in metal nitride alloy channels connecting the layers (c).

HAADF-STEM micrographs of Fig. 2. Here, the lower section of an as-deposited HfN/ScN superlattice stack (a) is compared with the similar region of samples annealed for 24 h (b) and 120 h (c). While the characteristic shape, thickness, and well-defined sharp interfaces of the individual metal and semiconductor layers within the lattice are maintained, the column boundaries clearly evolve during annealing.

The enlarged regions in the insets show that with annealing time the initial curvature (a) of the layers towards the substrate extends further down towards the substrate (b), and eventually a bridge connecting the layers of bright contrast (corresponding to the heavy Hf atoms) is formed right at the boundary. Noticeably, the layers stay well separated away from the boundaries.

Upon closer inspection, atomically resolved high-resolution STEM and EDX give an insight into the nature of the bridges. Figure 3a shows a more detailed STEM micrograph of a boundary of  $\text{Hf}_{0.5}\text{Zr}_{0.5}\text{N}/\text{ScN}$  after 120-h annealing at 950 °C and (b) an atomic resolution STEM micrograph of the rectangular region in (a). Individual (c) and combined (d) EDX maps confirm the Z-contrast interpretation of (b), assigning high-intensity regions to the  $\text{Hf}_{0.5}\text{Zr}_{0.5}\text{N}$  layers, with ScN appearing significantly darker.

Figure 3b shows that the lattice remains coherent and well ordered both across the metal/

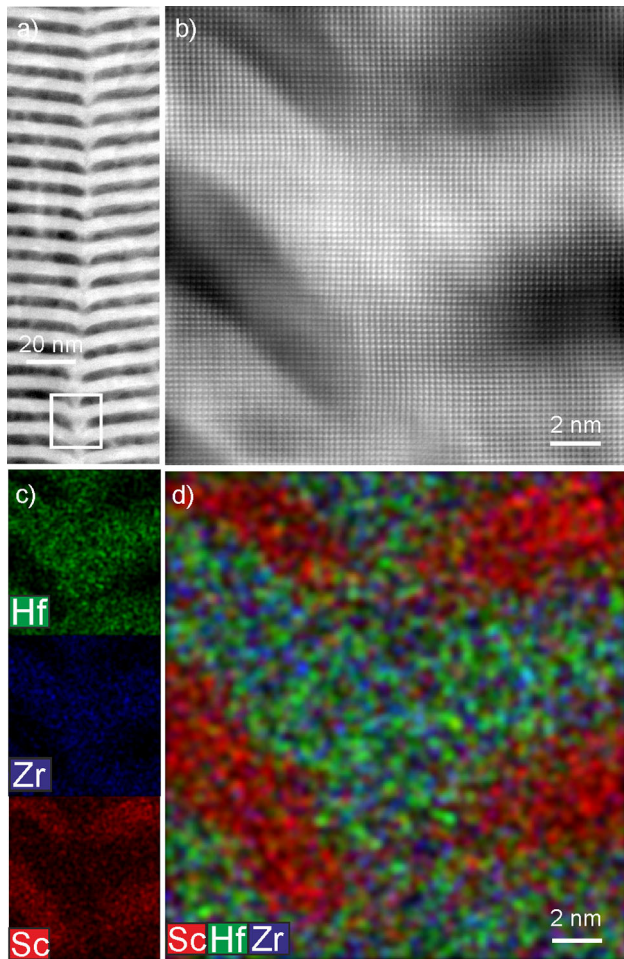


**Figure 3** HAADF-STEM micrographs of a column boundary of  $\text{Hf}_{0.5}\text{Zr}_{0.5}\text{N}/\text{ScN}$  after 120-h annealing at 950 °C in overview (a), and high resolution (b). Individual (c) and combined (d) EDX maps reveal that the bridge formed between the metal layers along the boundary comprises (Hf,Zr)N.

semiconductor interface as well as the boundary itself. The epitaxial character of the grown multilayers remains intact even though the layers bend almost vertically down towards the substrate along the boundaries and despite the formation of metal nitride bridges.

Furthermore, EDX results show that the bridge between the layers in a boundary channel comprises almost exclusively Zr and Hf (and N, not shown), giving rise to the assumption that the bridge is composed of rock salt  $\text{Hf}_{0.5}\text{Zr}_{0.5}\text{N}$ . These results are strengthened by quantification within selected regions of the maps in both regions, where hundreds of individual spectra within a boxed region were integrated for quantification (layers afar from the boundary vs. on the metal bridges), showing a

deviation of no more than 5 % in Zr and Hf content from the  $\text{Hf}_{0.5}\text{Zr}_{0.5}\text{N}$  stoichiometry, which is close to the accuracy limits for STEM-based EDX quantifications employing the  $k$  factor method using library  $k$  values.

Similarly, it is found that HfN bridges form in the HfN/ScN system, while ZrN bridges form in the ZrN/ScN system.

### Thermal stability

As mentioned above, prior annealing studies on metal/semiconductor superlattices that employed TiN as the metallic compound showed thermal instability by interdiffusion between the layers, which eventually led to a loss of the global superlattice structure [12]. As for the Zr- and Hf-based material systems discussed here, all three superlattice systems were thermally stable (i.e., no detectable diffusion of metal atoms in between the layers) under the exactly same annealing conditions that were used in the TiN(Al,Sc)N study (Figs. 4, 5, 6).

The lack of metal diffusion holds true for all parts of the samples throughout the full width of the superlattice stack as shown in the exemplary overview EDX map (raw data shown for better visibility

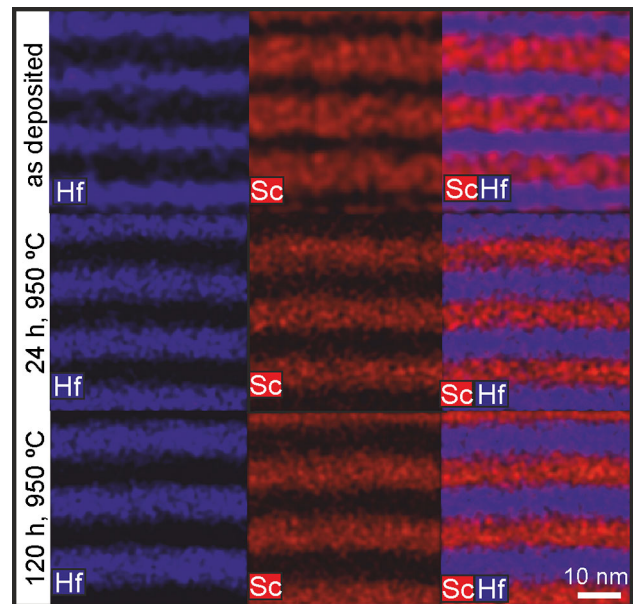


**Figure 4** Individual and combined EDX maps of HfN/ScN as deposited (upper row), and annealed at 950 °C for 24 h (middle row) and 120 h (lower row), showing well-separated layers both before and after heat treatment.

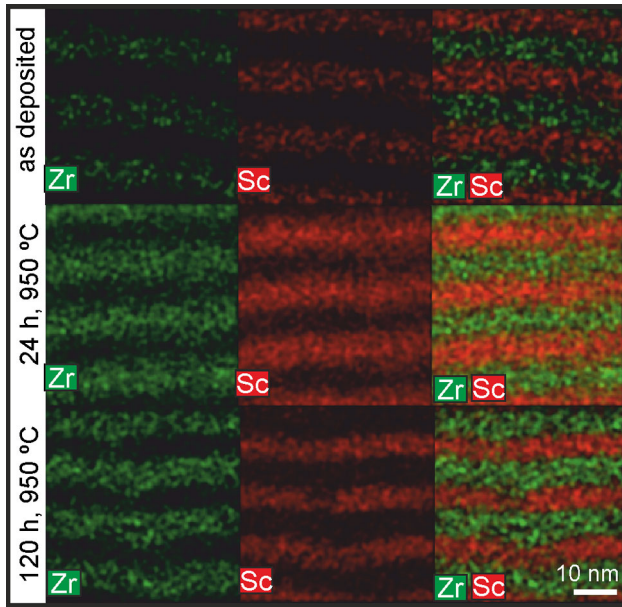


**Figure 5** Individual and combined EDX maps of ZrN/ScN as deposited (*upper row*), and annealed at 950 °C for 24 h (*middle row*) and 120 h (*lower row*), showing well-separated layers both before and after heat treatment.

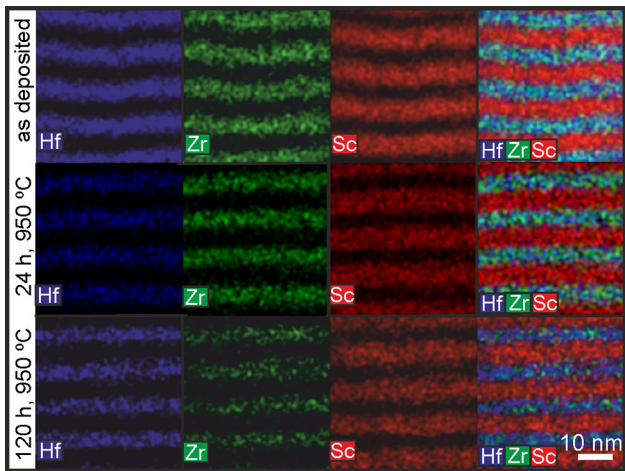


**Figure 6** Individual and combined EDX maps of Hf<sub>0.5</sub>Zr<sub>0.5</sub>N/ScN as deposited (*upper row*), and annealed at 950 °C for 24 h (*middle row*) and 120 h (*lower row*), showing well-separated layers both before and after heat treatment.

of exact interfaces position) of Hf<sub>0.5</sub>Zr<sub>0.5</sub>N/ScN in Fig. 7, with the only exceptions being the bridges formed along the column boundaries. As discussed in the previous section, these column boundaries occur a few hundreds of nanometers apart from each other and bridging occurs after long annealing treatments.

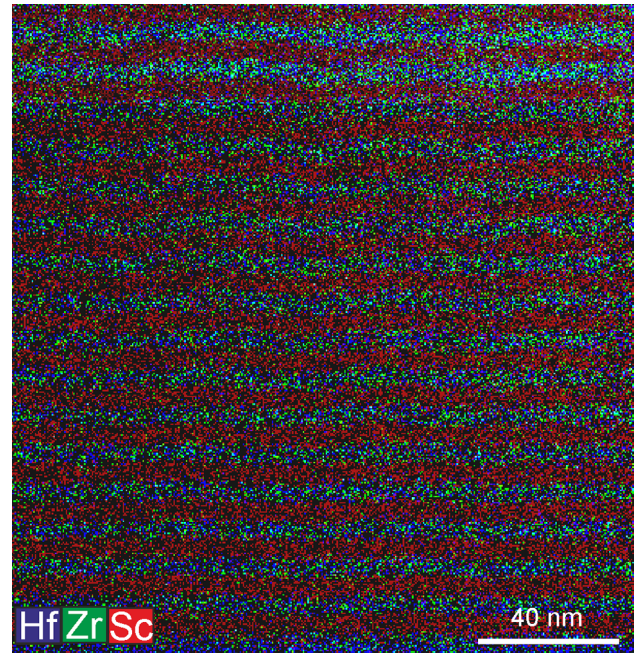


**Figure 7** Combined EDX map (raw data) of Hf<sub>0.5</sub>Zr<sub>0.5</sub>N/ScN after annealing at 950 °C for 120 h showing well-separated Hf<sub>0.5</sub>Zr<sub>0.5</sub>N metal and ScN semiconductor layers over large areas of the superlattice.

### Phase analysis

As discussed above, the cubic lattice of the rock salt metal nitride and rock salt semiconductor nitride appears coherent over large regions of the sample for all three material systems, confirming the high quality of the epitaxial growth. However, upon closer inspection of electron diffraction patterns (EDPs) from the entire 1- $\mu$ m-thick superlattice stack, faint and isotropic contrast rings can be found at well-defined distances that correspond to discrete d-spacings within the lattice.

Figure 8a shows an overview STEM micrograph of HfN/ScN after 120-h annealing treatment at 950 °C and the corresponding EDP in (b). Strikingly, the rings show d-spacings that cannot belong to the rock salt (B1) phase of HfN or ScN. The Fast Fourier Transform (FFT) of the lattice-resolved TEM micrograph of Fig. 8c shows the presence of intensity rings of the same d-spacings (measured values:  $\sim 3.4$ ,  $\sim 4.0$ ,  $5.6$ ,  $6.6$  nm<sup>-1</sup>). Masking out the main rock salt cubic reflections and performing inverse FFT indicates the regions where the faint rings originate, and HRTEM employing negative spherical aberration contrast imaging (NCSI) conditions by tuning the image corrector accordingly was applied there.

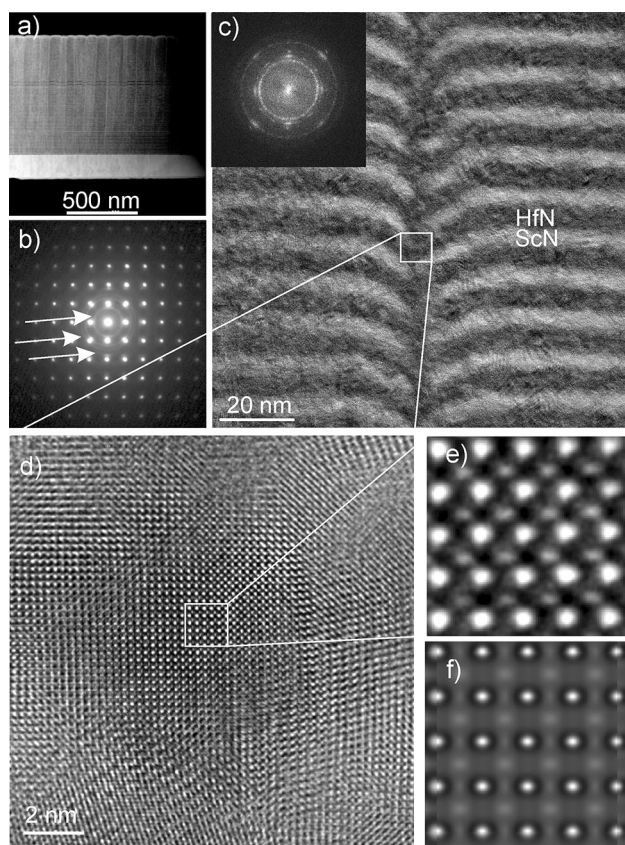


**Figure 8** Overview STEM micrograph of the entire HfN/ScN superlattice stack after 120 h of annealing (a), and EDP taken from that region (b). Faint intensity rings apart from the main rock salt phase cubic reflections are clearly visible. Rings with the same spacings appear in the FFT of a TEM micrograph taken from the region of a column boundary (c). HRTEM of details right inside the boundary reveals a grain of a few nm in diameter that corresponds to the zinc blende (B3) phase of HfN (d), as can be seen by comparing the d-spacings of the diffraction rings. Image intensity simulations assuming the B3 phase as structure model show a match between the experimental (e) and simulated (f) contrast features assuming realistic imaging parameters for objective lens and sample thickness.

Figure 8d shows an NCSI contrast micrograph with a grain exhibiting the particular lattice spacing almost exactly in zone axis, and by comparing the d-spacings with the literature it could be determined that this grain corresponds to the zinc blende HfN phase along [001], also referred to as B3 phase, with space group  $F\bar{4}3m$  and nominal low-index d-spacings of  $3.4503 \text{ nm}^{-1}$  {111},  $3.9841 \text{ nm}^{-1}$  {200},  $5.6343 \text{ nm}^{-1}$  {220}, and  $6.6068 \text{ nm}^{-1}$  {311}. Comparing details of the experimental image (e) with a multislice simulation (f) assuming the B3 phase along [001], objective lens settings producing NCSI contrast image for our

Titan<sup>3</sup> microscope ( $C_s = -7 \mu\text{m}$ ,  $Z = +4 \text{ nm}$ ), and residual aberrations for astigmatism and coma according to the corrector tunings, the HfN B3 phase was confirmed. Furthermore, EDX quantification from maps of regions exhibiting the zinc blende grains (not shown here) confirm the stoichiometry.

Similar analysis was done for the long-time annealed ZrN/ScN and  $\text{Hf}_{0.5}\text{Zr}_{0.5}\text{N}/\text{ScN}$  samples, showing that similar zinc blende phases with ZrN and (Hf,Zr)N stoichiometry, respectively, are formed. FFT analysis employing masking and inverse transforming shows that the typical size of zinc blende grains is below 5 nm in diameter as in Fig. 8d. The zinc blende grains appear faceted with low-energy atomic planes forming the surfaces, and these grains preferably appear at the interfaces between the metal and semiconductor nitride layers or in the vicinity of the columnar boundaries, but not inside the ScN layers. Moreover, as can be seen from the EDPs, the zinc blende grains exhibit homogeneously random orientation relationships with respect to the host rock salt lattice.

Rock salt-to-zinc blende phase transformations in transition metal nitrides are discussed in the literature and are said to happen under pressure. Theoretical calculations for the ZrN and HfN material systems show that rock salt is the energetically more stable and thus preferred phase assuming exact stoichiometry [25]. These theoretical calculations are reflected in our findings since zinc blende grains appear only sparsely within the superlattice. Investigations of the origin and formation of the zinc blende phase can be a matter of future investigations.

## Conclusions

Detailed TEM-based analysis of the film quality, morphology, microstructural evolution under annealing, and thermal stability of the three magnetron-sputtered metal/semiconductor superlattices [HfN/ScN, ZrN/ScN, and  $(\text{Hf}_{0.5}\text{Zr}_{0.5})\text{N}/\text{ScN}$ ] has been performed.

It was shown by EDX mapping in probe-corrected STEM mode that although columnar boundaries originating from defects at the substrate–film interface and forming under long-time annealing to 950 °C allow for transport of atomic species from the metallic layers perpendicular to the superlattice stack, no diffusion of atomic species in between the

metal and semiconductor layers is observed as in previous TiN-based systems [12], keeping the multi-layer morphology intact over areas of a few hundred nanometers and throughout its entire thickness.

The films are of high epitaxial quality, show mostly flat interfaces disturbed by columnar boundaries about every 100 nm on average, and comprise the cubic rock salt phase, with the exception of nanometer-size inclusions formed by transition metal nitride zinc blende phases that were identified in low quantities. Their origin is unclear at the moment.

Our results show the feasibility of growing high-quality metal/semiconductor superlattice stacks based on Zr and Hf nitrides by magnetron sputtering, and the TEM investigations demonstrate that due to the thermal stability of the three different systems, these superlattices are well suited for applications in thermoelectric materials, plasmonics, and hard coatings.

## Acknowledgements

The Knut and Alice Wallenberg (KAW) Foundation is acknowledged for the Electron Microscope Laboratory in Linköping. M.G., L.H., J.L.S., and J.B. acknowledge the financial support from the Swedish Research Council [RÅC Frame Program (2011-6505), Project Grant 2013-4018, and Linnaeus Grant (LiLi-NFM)] as well as the Swedish Government Strategic Research Area in Materials Science on Functional Materials at Linköping University (Faculty Grant SFO-Mat-LiU 2009-00971). B.S. and T.D.S. acknowledge the financial support from the National Science Foundation and the U.S. Department of Energy (Award No. CBET-1048616).

**Author contributions** The manuscript was written through contributions of all authors. All authors have provided approval to the final version of the manuscript.

## Compliance with ethical standards

**Conflict of interest** None.

## References

- [1] Jaklevic RC, Lambe J (1966) Molecular vibration spectra by electron tunneling. *Phys Rev Lett* 17(22):1139–1140
- [2] Jaklevic RC, Lambe J (1975) Experimental study of quantum size effects in thin films by electron tunneling. *Phys Rev Lett* 12(10):4146–4160
- [3] Sands T (1988) Stability and epitaxy of NiAl and related intermetallic films on III–V compound semiconductors. *Appl Phys Lett* 52:197–199
- [4] Palmstrøm CJ, Tabatabaie N, Allen SJ Jr (1988) Epitaxial growth of ErAs on (100)GaAs. *Appl Phys Lett* 53:2608–2610
- [5] Sands TD, Palmstrøm CJ, Harbison JP, Keramidias VG, Tabatabaie N, Cheeks TL, Silberberg Y (1990) Stable and epitaxial metal/III–V semiconductor heterostructures. *Mater Sci Rep* 5:98–170
- [6] Krishnamurthy HNS, Jacob Z, Narimanov EE, Kretzschmar I, Menon VM (2012) Topological transitions in metamaterials. *Science* 336:205–209
- [7] Saha B, Saber S, Naik GV, Boltasseva A, Stach EA, Kvam EP, Sands TD (2015) Development of epitaxial  $\text{Al}_x\text{Sc}_{1-x}\text{N}$  for artificially structured metal/semiconductor superlattice metamaterials. *Phys Status Solidi B* 252(2):251–259
- [8] Saha B, Lawrence SK, Schroeder JL, Birch J, Bahr DF, Sands TD (2014) Enhanced hardness in epitaxial TiAlScN alloy thin films and rocksalt TiN/(Al, Sc)N superlattices. *Appl Phys Lett* 105:151904–151905
- [9] Saha B, Rui Koh Y, Comparan J, Sadasivam S, Schroeder JL, Garbrecht M, Birch J, Cahill D, Fisher T, Shakouri A, Sands TD (2016) Cross-plane thermal conductivity of (Ti, W)N/(Al, Sc)N metal/semiconductor superlattices. *Phys Rev B* 93:045311–045321
- [10] Naik GV, Saha B, Liu J, Saber SM, Stach E, Irudayaraj JMK, Sands TD, Shalaev VM, Boltasseva A (2014) Epitaxial superlattices with titanium nitride as a plasmonic component for optical hyperbolic metamaterials. *Proc Natl Acad Sci* 111:7546–7551
- [11] Saha B, Naik GV, Saber S, Stach E, Shalaev VM, Boltasseva A, Sands TD (2014) TiN/(Al, Sc)N metal/dielectric superlattices and multilayers as hyperbolic metamaterial in the visible spectral range. *Phys Rev B* 90:125420–125432
- [12] Schroeder JL, Saha B, Garbrecht M, Schell N, Sands TD, Birch J (2015) Thermal stability of epitaxial cubic-TiN/(Al, Sc)N metal/semiconductor superlattices. *J Mater Sci* 50:3200–3206
- [13] Zebarjadi M, Bian ZX, Singh R, Shakouri A, Wortman R, Rawat V, Sands TD (2009) Thermoelectric transport in a ZrN/ScN superlattice. *J Electron Mater* 38:960–963
- [14] Shakouri A, Zebarjadi M (2009) Nanoengineered materials for thermoelectric energy conversion. In: Volz S (ed) *Thermal nanosystems and nanomaterials*. Springer, Berlin, pp 225–299
- [15] Norrby N, Johansson MP, M'saoubi R, Oden M (2012) Pressure and temperature effects on the decomposition of arc

- evaporated  $\text{Ti}_{0.6}\text{Al}_{0.4}\text{N}$  coatings in continuous turning. *Surf Coat Technol* 209:203–207
- [16] Carvalho SR, Silva S, Machado AR, Guimaraes G (2006) Temperature determination at the chip-tool interface using an inverse thermal model considering the tool and tool holder. *J Mater Process Technol* 179:97–104
- [17] Jia CL, Lentzen M, Urban K (2003) Atomic-resolution imaging of oxygen in perovskite ceramics. *Science* 299:870–873
- [18] Lentzen M (2004) The tuning of a Zernike phase plate with defocus and variable spherical aberration and its use in HRTEM imaging. *Ultramicroscopy* 99:211–220
- [19] Garbrecht M, Spiecker E, Jäger W, Tillmann K (2008) Aberration-corrected HRTEM of the incommensurate misfit layer compound  $(\text{PbS})_{1.14}\text{NbS}_2$ . *Mater Res Soc Symp Proc* 1026E:C10–C11
- [20] Spiecker E, Garbrecht M, Jäger W, Tillmann K (2009) Advantages of aberration correction for HRTEM investigation of complex layer compounds. *J Microsc* 237(3):341–346
- [21] Garbrecht M, Spiecker E, Tillmann K, Jäger W (2011) Quantitative atom column position analysis at the incommensurate interfaces of a  $(\text{PbS})_{1.14}\text{NbS}_2$  misfit layered compound with aberration-corrected HRTEM. *Ultramicroscopy* 111:245–250
- [22] Stadelmann P (1987) EMS—a software package for electron diffraction analysis and HREM image simulation in materials science. *Ultramicroscopy* 21:131–145
- [23] Hultman L, Wallenberg LR, Shinn M, Barnett SA (1992) Formation of polyhedral voids at surface cusps during growth of epitaxial TiN/NbN superlattice and alloy films. *J Vac Sci Technol A* 10(4):1618–1624
- [24] Wallenberg LR, Hultman L, Shinn M, Barnett SA (1992) HREM of voids in TiN/NbN superlattices. In: *Electron microscopy, vol 2, EUREM 92, Granada, Spain*, pp 755–756
- [25] Chen W, Jiang JZ (2010) Elastic properties and electronic structures of 4d- and 5d-transition metal mononitrides. *J Alloys Compd* 499:243–254